

PHYS4620 Senior Project II

Simulation of Rossby Wave Instability in the Accretion Disks

Man Tsun, Wu

Department of Physics, The Chinese University of Hong Kong, Shatin, New Territories, Hong Kong

(Dated: April 2020)

Rossby wave instability (RWI) could be a mechanism for the angular momentum transport in the protoplanetary disk, as suggested by Lovelace et al. (1999). Numerical simulations were conducted to verify the existence of RWI by adding a planet to an inviscid 2D disk. The system could lead to favourable condition for RWI to occur, which created an extremum of the key function \mathcal{L} related to the radial profile of vorticity. As a results, vortices are formed in the edges of planetary gaps and facilitate planetismals growth. The results of the formation and evolution of vortices and planetary gaps were discussed. Different thermal relaxation timescales were used to observe the effect on the efficiency of angular momentum transport. Variations of the simulation were suggested and the instability could be quantitatively verified in the future.

I. INTRODUCTION

The planet formation has been a highly discussed topic and there are theories that why the protoplanetary disk related to the formation process have gaps and vortices. However, due to the limitation of precise measurements, there are still a lot of uncertainties in our understanding of the mechanism. In this project, Rossby wave instability (RWI) was investigated, which could be a mechanism to transport angular momentum to accrete matter in a protoplanetary disk.

Rossby waves, equivalent to planetary waves, could be found in the atmosphere or oceans in planets (Lovelace & Romanova, 2013). The topic has been studied in both meteorology and astronomy.

For a non-self gravitating Keplerian disk, Rossby wave instability could be triggered when there is a local extremum in the radial profile, of the quantity \mathcal{L} , related to the potential vorticity and the entropy at certain radius (Lovelace et al., 1999). RWI can occur in the dead zone where the ionization level is too low for magnetising effect, such as magnetorotational instability (Tagger & Varnière, 2006). Assuming the disk is geometrically thin, the theory has been verified by various numerical simulations in 2D and 3D with different methods, such as inducing a planet into the disk or setting a perturbed density profile (Lobo Gomes et al., 2015; Les & Lin, 2015; Meheut et al., 2012; Meheut et al., 2010).

In order to study the mechanism, 2D hydrodynamics (HD) simulations were performed to verify the existence and effects of the Rossby wave instability of the geometrically thin accretion disks under disk-planet interaction. The vertical motions assumed to be small such that 2D simulations with vertically integrated quantities are good approximations. The PLUTO code, which is a useful software to solve fluid dynamics equations was utilized to perform the simulations (Mignone et al., 2007).

The paper is structured as follows: Section II introduces the accretion disk and the theory of Rossby wave instability; Section III introduces the method and governing equations of the simulations; Section IV verifies and

validates the numerical code; Section V presents and discusses simulation results; and Section VII concludes the results and the states the outlook of further studies.

II. THE ACCRETION DISK AND THE ROSSBY WAVE INSTABILITY

The protoplanetary accretion disk is believed to originate from a spherical cloud which consists of mainly gases such as hydrogen and helium (Lin & Marcus, 2002). They are formed after the collapse of a rotating spherical cloud under the gravitational pull of its central star. The surrounding dust will eventually accumulate and form a thin protoplanetary disk, which is responsible for planet formation. Recently, planet formation was captured around a young star called HL Tauri by the ALMA radio telescope (Jonathan, 2014) as shown in figure 1. Radio waves were collected through 66 antennas and combined through interferometry. Concentric rings and planetary gaps are observed, which could be the hint of the planet orbiting around the central star.

The accretion disk is treated as a geometrically thin disk in this paper, since the thickness h of the disk is much smaller than the size of the disk. A 2D disk is considered for simplicity and the results could be extrapolated to the 3D case (Meheut et al. 2012). In such a disk, the pressure P considered is the vertically integrated pressure and Σ is the surface mass density, where

$$P(r) = \int_{-h}^h p(r, z) dz, \quad (1)$$

and

$$\Sigma(r) = \int_{-h}^h \rho(r, z) dz, \quad (2)$$

where r is the radius from the center of disk and z is the vertical direction. For an equilibrium disk with an central star with mass M_{star} , the self-gravity could be negligible since the mass of the central star is large compared to the

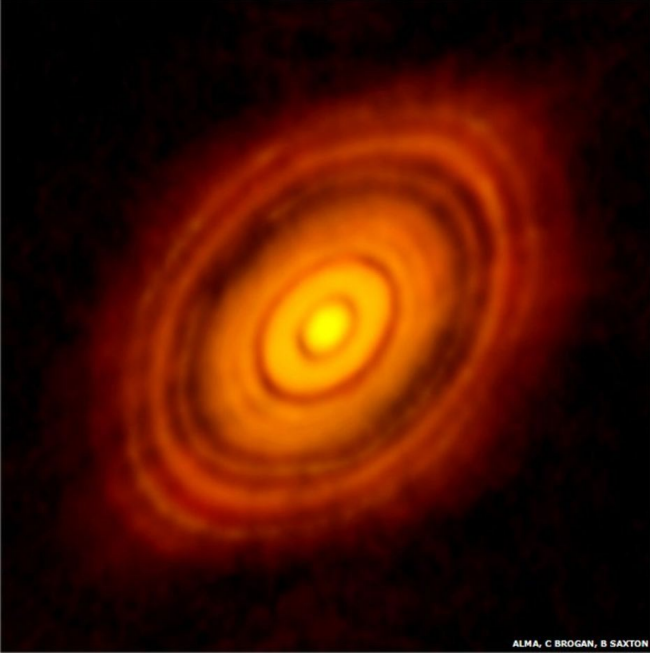


FIG. 1: The HL Tauri protoplanetary disk captured by ALMA (Brogan C, & Saxton B., 2014).

disk, which could be proved in the protoplanetary disk captured by ALMA in figure 1. The central star could be treated as a point mass as the size of the disk is large. The disk is also assumed to be stationary and axisymmetric, with negligible radial velocity v_r . By balancing the gravitational force and the force due to pressure gradient with centrifugal force, the azimuthal velocity v_ϕ for the disk in hydrostatic equilibrium could be determined by

$$\frac{v_\phi^2}{r} = \frac{1}{\Sigma} \frac{dP}{dr} + v_K^2, \quad (3)$$

where $v_K = \sqrt{\frac{GM_{star}}{r}}$ is the Keplerian velocity and G is the gravitational constant. Assuming the gas is ideal in the disk, the equation of state suggests that

$$c_s^2 = \gamma \frac{P}{\Sigma}, \quad (4)$$

where c_s is the speed of sound and γ is the adiabatic index.

The RWI of a geometrically thin, inviscid, nonmagnetised accretion disk could be related by the quantity:

$$\mathcal{L}(r) \equiv \frac{\Sigma^{1-\gamma} P}{2(\nabla \times \mathbf{v}) \cdot \hat{\mathbf{z}}}, \quad (5)$$

where \mathbf{v} is the velocity vector (Li et al., 2000). The extremum occurs in the edges “dead zone” of the accretion disk, where the ionization level is too low for the magnetisation effect to occur.

The dispersion relation could be written in terms of

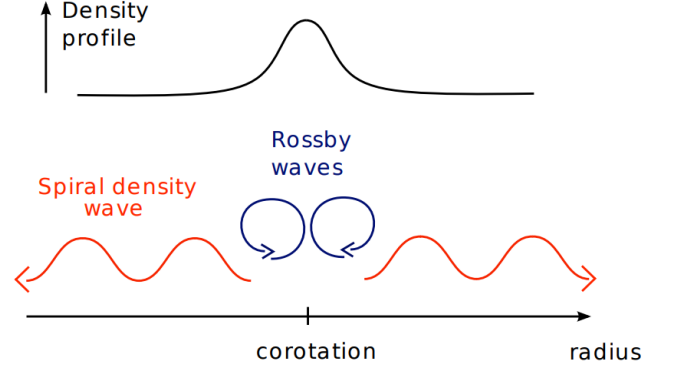


FIG. 2: The schematic view of the RWI (Lovelace & Romanova, 2013).

the wave frequency in the rotating frame $\bar{\omega} \equiv \omega - m\Omega$:

$$\bar{\omega} = -\frac{m\alpha c_s^2}{c_s^2(k^2 + m^2/r^2) + r^2\kappa^2}, \quad (6)$$

where ω is the wave frequency, m is the wavenumber in azimuthal direction, k is the wavenumber in radial direction, α is the vorticity gradient and $\kappa \equiv 4\Omega^2 + 2r\Omega \frac{\partial\Omega}{\partial r}$ is the epicyclic frequency where Ω is the rotation frequency.

Figure 2 shows the schematic view of the RWI. In the linear phase of RWI, Rossby waves are emitted on both sides from the corotation radius r_c and results in exponentially growing vortices, where r_c is located at the maximum of the density profile according to eq (5). For $r > r_c$, the energy flux is positive, so that the gas outside r_c gains angular momentum and moves outward. In contrast, for $r < r_c$, the gas loses angular momentum and moves inward, leading to accretion of mass (Lovelace & Romanova, 2013).

Physically, the instability-induced viscosity enhances the exchange of energy and angular momentum between the gas at different radii. For instant, angular momentum is transported outwards and mass is accreted towards the center because the matter with slower v_ϕ will move to a smaller radius of the Keplerian orbit, until no such orbit in Newtonian mechanics.

There are a number of possible ways to generate an extremum in \mathcal{L} . The method used here is to introduce a small planet to the disk which created a density bump for RWI to occur.

III. THE SIMULATION METHOD AND DESIGN

PLUTO code is an astrophysical fluid code designed for direct numerical simulations. It provides a multiphysics, multialgorithm and user friendly environment to solve the system of conservation laws (Mignone, 2007). Attributes such as the boundary conditions, the geometry,

the body force and physics module etc. could be set manually to define a specific problem. The HD module was utilized for the RWI simulation in this study.

A. Initialization

The simulation method followed the design of planet-disk interaction for RWI by Lobo Gomes et al. (2015), where a relatively small planet with mass M_p was added gradually within the first period of the Keplerian orbit into a Keplerian disk with a central star of mass M_{star} , in order to avoid big disturbance to the system.

For the equilibrium Keplerian disk with a central star initialized in the simulation, the surface density, pressure profile and the velocity vector are defined initially. Polar coordinates are chosen for the initially axisymmetric disk. The surface density profile $\Sigma(r)$ is given by

$$\Sigma(r) = \Sigma_0 \left(\frac{r}{r_0} \right)^{-\beta_\Sigma}, \quad (7)$$

where $r_0 = 1$ AU, $\Sigma_0 = 10^{-4} \text{ M}_\odot/\text{AU}^2$ and $\beta_\Sigma = 1.5$.

The pressure profile is determined using eq (4) where $\gamma = 1.4$ and $c_s(r)$ is given by

$$c_s(r) = c_0 \left(\frac{r}{r_0} \right)^{\beta_T/2}, \quad (8)$$

where $c_0 = 0.05v_K$ and $\beta_T/2 = 0.5$. c_0 is related to the Keplerian velocity v_K such that the initial aspect ratio $h = H/r = 0.05$, where the scale height is defined as $H \approx c_s r / v_K$ (Bambi, 2016).

The radial velocity v_r is set to zero and the azimuthal velocity v_ϕ is governed by eq (3), such that

$$v_\phi = \sqrt{v_K^2 + c_s^2 \frac{-\beta_\Sigma - \beta_T}{\gamma}}. \quad (9)$$

A planet with mass M_p was introduced to the disk to create the density bump to trigger the RWI. To avoid large disturbance, the planet was slowly added along the first orbital period $\mathcal{P} = 2\pi \left(\frac{GM_{star}}{|\mathbf{R}_p|^3} \right)^{-1/2}$, where $|\mathbf{R}_p|$ is the location of the planet from center of the disk. In the first orbit, the planet mass M'_p was set to be a fraction of its final mass at time t , is given by

$$M'_p = M_p \left[\sin \left(\frac{\pi t}{2 \mathcal{P}} \right) \right]^2. \quad (10)$$

Initially, the planet was placed at $(r, \theta) = (r_0, 0)$ with velocity vector $(v_r, v_\theta) = \left(0, \sqrt{\frac{GM_{star}}{|\mathbf{R}_p|}} \right)$.

The masses are given in units of solar mass M_\odot , where $M_{star} = 1 \text{ M}_\odot$ and $M_p = 1 \text{ M}_J = 0.0009543 \text{ M}_\odot$, where M_J is the mass of Jupiter. The distances are in AU, the surface densities in $\text{M}_\odot/\text{AU}^2$ and the velocities in $v_K(r_0)$ AU/yr, such that $G = 1 \text{ AU}^3\text{yr}^{-2}\text{M}_\odot^{-1}$. The grids for

radial and azimuthal direction are both uniform and the resolution is 256×256 . The computational domain are $(0.25, 4.0)$ and $(0, 2\pi)$ in radial and azimuthal direction respectively.

B. Time evolution

The evolution of the system is governed by the following three fluid dynamics equation:

$$\frac{\partial \Sigma}{\partial t} + \nabla \cdot (\Sigma \mathbf{v}) = 0, \quad (11)$$

$$\frac{\partial \mathbf{v}}{\partial t} + \mathbf{v} \cdot \nabla \mathbf{v} = -\frac{\nabla P}{\Sigma} - \nabla \Phi_g, \quad (12)$$

and

$$\frac{\partial P}{\partial t} + \mathbf{v} \cdot \nabla P + \Sigma c_s^2 \nabla \cdot \mathbf{v} = 0. \quad (13)$$

Eq (11), eq (12) and eq (13) refer to the conservation of mass, conservation of momentum and conservation of energy of the inviscid and adiabatic fluid respectively (Thompson, 2006). The equations were derived using the basic equations of fluid dynamics and the equation of state. Φ_g is the gravitational potential, which is determined by

$$\Phi_g = -\frac{GM_p}{\sqrt{|\mathbf{r} - \mathbf{R}_p|^2 + \epsilon^2}} - \frac{GM_{star}}{|\mathbf{r}|}, \quad (14)$$

where ϵ is a softening parameter to avoid numerical divergence when $|\mathbf{r} - \mathbf{R}_p|$ is close to zero, and is given by

$$\epsilon = k_\epsilon H \approx k_\epsilon R_H, \quad (15)$$

where H is the local scale height, $R_H = |\mathbf{R}_p| [M_p / (3M_{star})]^{1/3}$ is the Hill radius in the Hill sphere and k_ϵ is a coefficient. The Hill sphere is considered in the disk where the mass of the star is much greater than the planet. R_H could be determined by balancing the total gravitational force from the interactions and the centrifugal force in the hill sphere. Moreover, eq (15) is given by simulations such that the 3D effects of vertical density variations could be recovered. With negligible self gravity since the disk mass is much smaller than the mass of star M_{star} , k_ϵ is determined as 0.6 by numerical simulations, such that 3D effects could be approximated well (Müller et al., 2012).

Thus, P , Σ and \mathbf{v} were updated for every time steps Δt , which is determined by the Courant-Friedrichs-Lewy (CFL) condition. Δt is related to the grid spacing for accurate results due to the CFL condition for convergence.

The planet updated its position for every fluid dynamic steps by the gravitational force from both the star and

the disk. The total gravitational acceleration \mathbf{a}_p is given by

$$\mathbf{a}_p = -\frac{GM_{star}\mathbf{R}_p}{|\mathbf{R}_p|^3} + \xi \int_{disk} \frac{G\Sigma(\mathbf{r} - \mathbf{R}_p)}{\sqrt{(|\mathbf{r} - \mathbf{R}_p|^2 + \epsilon^2)^3}} dA, \quad (16)$$

where dA is the area element,

$$\xi = 1 - \exp \left[-\frac{|\mathbf{r} - \mathbf{R}_p|^2}{(0.06R_H)^2} \right] \quad (17)$$

is another factor to soften the contribution of second term from the disk-planet interaction due to the system in the Hill sphere. The position of the planet was updated using the leapfrog integrator, which is a second-order method to compute the movement due to acceleration of a particle. The method conserves energy and the total energy is the same if the mass is conserved. The time stepping is given by

$$\mathbf{v}_{p,i+1/2} = \mathbf{v}_{p,i} + \frac{1}{2}\mathbf{a}_{p,i}\Delta t, \quad (18)$$

$$\mathbf{R}_{p,i+1} = \mathbf{R}_{p,i} + \mathbf{v}_{p,i+1/2}\Delta t \quad (19)$$

and

$$\mathbf{v}_{p,i+1} = \mathbf{v}_{p,i+1/2} + \frac{1}{2}\mathbf{a}_{p,i+1}\Delta t, \quad (20)$$

where i is the current step, $i + 1/2$ is the next half step, $i + 1$ is the next step and \mathbf{v}_p is the velocity vector of the planet.

The disk was evolved using eq (11), eq (12) and eq (13) with the gravitation potential governed by eq (14), then the planet position is updated using eq (18), eq (19) and eq (20).

With the choice of units, one orbital period is equal to 2π years and 500 periods were simulated. Out-flow boundary conditions were used in the radial direction and periodic conditions in the azimuthal direction. Spacial integration and time evolution were performed using the piecewise parabolic method and second order Runge-Kutta schemes respectively with simple Lax-Friedrichs scheme.

C. Thermal relaxation

When RWI occurs, heat will accumulate and retain in the disk if there is no radiative effects. Cooling could be applied in order to account heat transfer when the pressure is built up. The first-order thermal relaxation was implemented in order to model the system cooling:

$$\frac{dT}{dt} = -\frac{T - T_0}{\tau}, \quad (21)$$

where T is the temperature at certain time t , T_0 is the initial temperature and τ is the thermal relaxation time

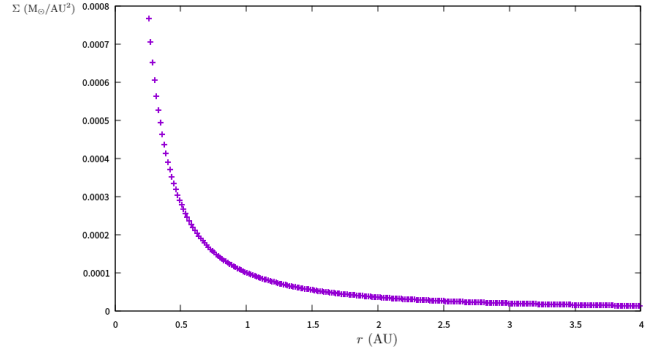


FIG. 3: The initial surface density radial profile of eq (7).

scale. τ could be varied in order to control the speed of thermal relaxation. For instant, for $\tau \rightarrow \infty$, the radiative effects are neglected and the system is totally adiabatic. For $\tau \rightarrow 0$, the thermal relaxation tends to be infinitely efficient, which corresponds to the isothermal case.

Using the relation $T \propto \frac{P}{\Sigma}$, eq (21) could be written in terms of pressure. In terms of the numerical time step Δt , the pressure could be updated after every fluid dynamics equation integration steps using eq (11), eq (12) and eq (13), by

$$P_{new} = P_{old} - \frac{\Delta t}{\tau} \left(P_{old} - P_0 \frac{\Sigma}{\Sigma_0} \right), \quad (22)$$

where P_{new} is the new pressure from the relaxed temperature, P_{old} is the pressure from eq (13), P_0 is the initial pressure, Σ is the surface density from eq (11) and Σ_0 is the initial surface density. Eq (22) is only valid for $\tau > 0$, corresponding to the non-isothermal cases. For $\tau = 0$, c_s was kept constant throughout the simulation and P was updated in every step using eq (4), such that the disk was locally isothermal.

IV. CODE CONTROL AND VALIDATION

A. initialization

Figure 3, figure 4, figure 5 and figure 6 show the initial profiles of the variables, assuming the disk is axisymmetric initially.

Figure 7 shows the curve of M'_p against \mathcal{P} . The planet was gradually added to the disk and the disk-planet interaction became more significant afterwards.

B. The Leapfrog Integrator

The time marching algorithm of the planet is given by eq (18), eq (19) and eq (20) with acceleration due to the gravity of disk and star given by eq (16). Analytical results were expected if the planet-disk interaction was

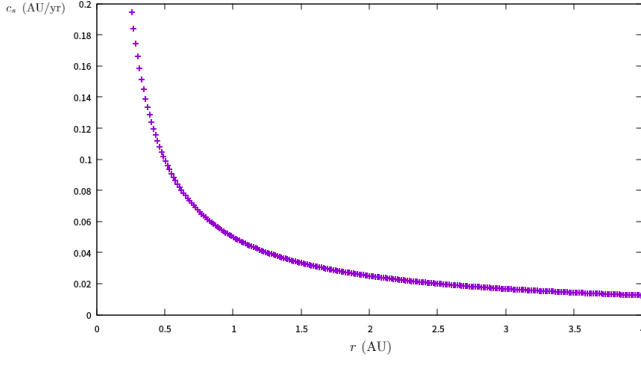


FIG. 4: The initial sound speed radial profile of eq (8).

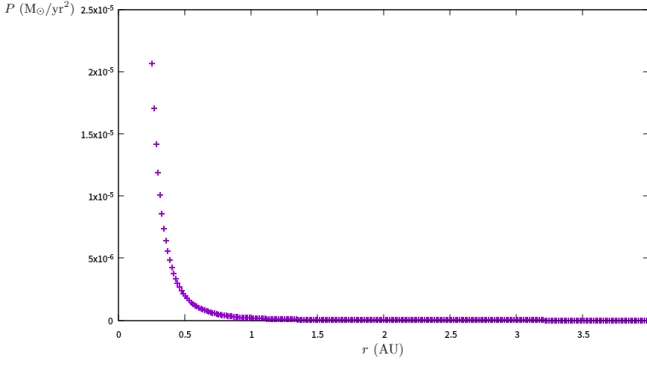


FIG. 5: The initial pressure radial profile of eq (4).

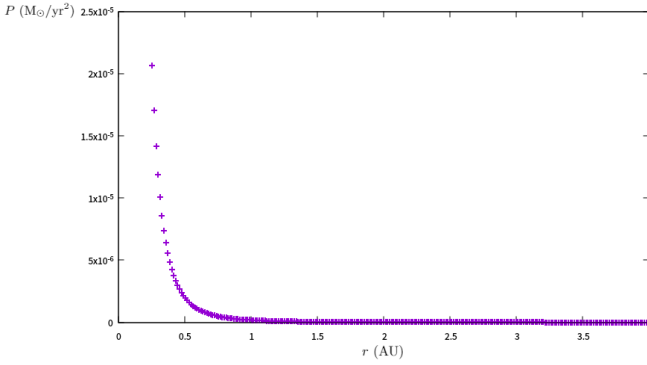


FIG. 6: The initial azimuthal velocity profile of eq (9).

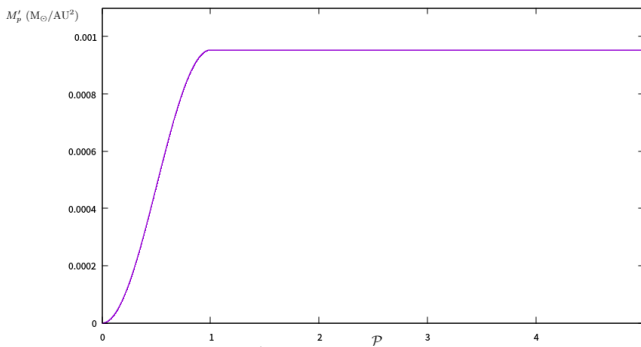


FIG. 7: The plot of planet mass M'_p against the orbital period of the disk \mathcal{P} .

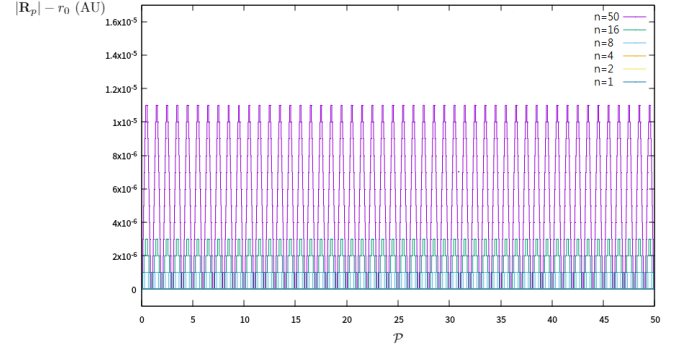


FIG. 8: The plots of the radial positions of the planet $|\mathbf{R}_p|$ against the orbital period of the disk \mathcal{P} using different temporal resolutions n of leapfrog integrator without the planet-disk interaction.

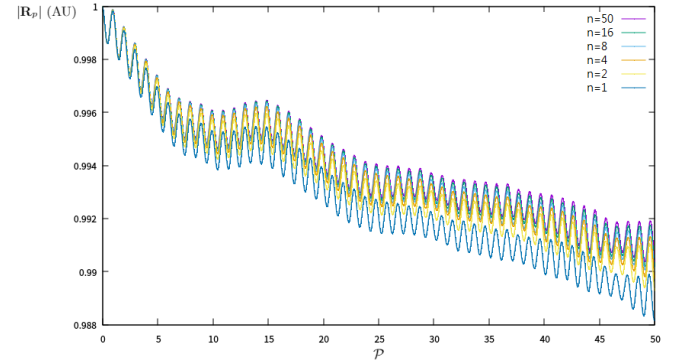


FIG. 9: The plots of the radial positions of the planet $|\mathbf{R}_p|$ against the orbital period of the disk \mathcal{P} using different temporal resolutions n of leapfrog integrator including the planet-disk interaction.

ignored. Figure 8 shows the deviation from the exact solution along the orbit without the planet-disk interaction, where n is the number of leapfrog integrator steps for every fluid dynamics integration steps. It shows that the planet was simply in Keplerian orbit with constant $|\mathbf{R}_p|$, and the integration with smaller n had extremely small deviation from the analytic results, only due to the precision of the program. Figure 9, the graph of $|\mathbf{R}_p|$ against \mathcal{P} with the planet-disk interaction, shows that higher resolution of the leapfrog integrator had smaller deviation from the Keplerian orbit. Figure 10 shows the curves of total energies of the planet against \mathcal{P} . Figure 10 shows results agree to the conservation of energy, while figures 10(c) and (d) show that the planet was losing energy. This could be explained by the outflow boundary conditions of the system and the total disk mass decreases with time. In order to study the total mass in different orbits, the system was simulated again in reflective boundary condition in radial direction without the planet added, which is expected to have constant mass throughout the simulation. Figure 11 shows that the total mass of the simulations of the planet-disk system

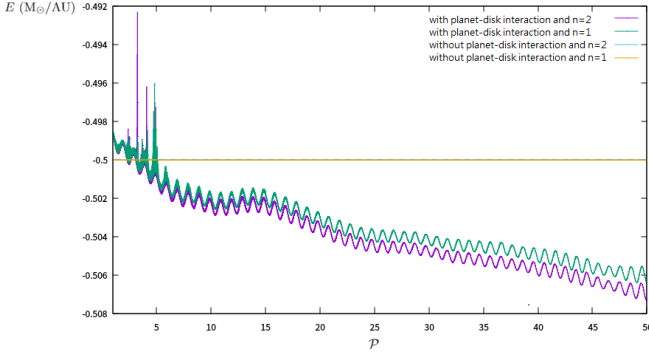


FIG. 10: The plots of the total energies of the planet against the orbital period of the disk \mathcal{P} with different variations.

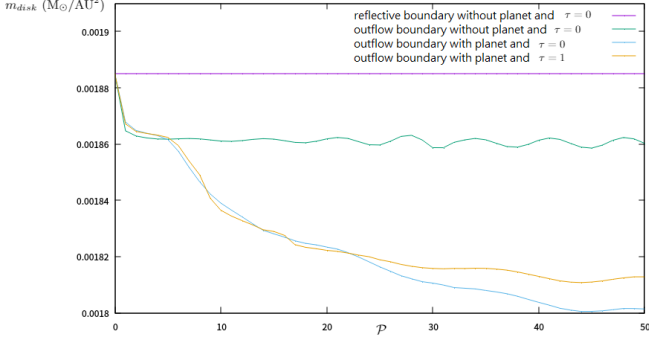


FIG. 11: The plots of the total mass of the disk against the orbital period \mathcal{P} .

decreased with time if the outflow boundary conditions was used. Without adding the planet, the total mass was constant if reflective boundaries in radial direction was used, while the outflow boundary condition allows matter to flow into the ghost zone beyond the boundary, as more matter could be transported away from the disk through the inner boundary.

C. The thermal relaxation

The thermal relaxation timescale could be varied from zero to infinity, corresponding to the fully isothermal case and the fully adiabatic case respectively. The former introduces the constant sound speed c_s for every time step t while the latter ignored the thermal relaxation. In the simulation, different τ s were verified to observe the effects of the efficiency of the thermal relaxation.

Figure 12 shows the curves of the differences of total disk mass Δm between the simulation without using thermal relaxation and different τ s. It shows that simulation result is the most similar with the case of $\tau = 10000$, which was expected to be similar to the adiabatic condition.

Figure 13 shows the curves of the differences of total

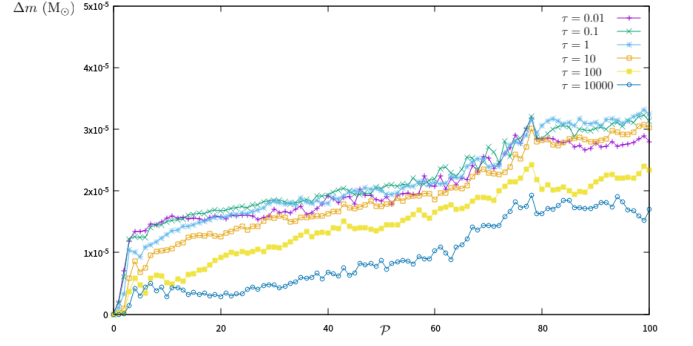


FIG. 12: The plots of the differences of total disk mass Δm between the result of the algorithm without thermal relaxation and the algorithms with different thermal relaxation timescales τ against the orbital period of the disk \mathcal{P} .

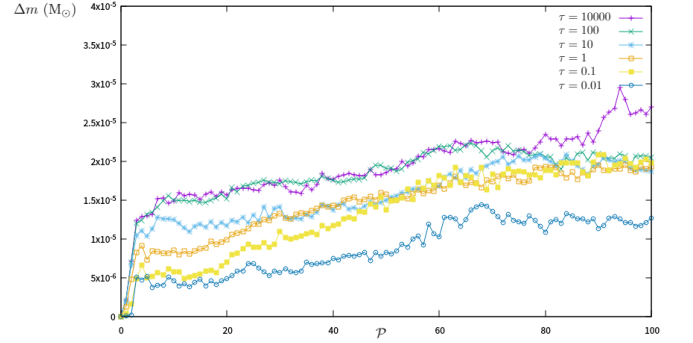


FIG. 13: The plots of the differences of total disk mass Δm between the isothermal case and the algorithms with different thermal relaxation timescales τ against the orbital period of the disk \mathcal{P} .

disk mass Δm between the isothermal case and different τ s. It shows that simulation result is the most similar with the case of $\tau = 0.01$, which was expected to be similar to the isothermal condition.

V. SIMULATION RESULTS AND DISCUSSION

Figure 14 shows the graphs of the evolution of surface density perturbation $\frac{\Sigma}{\Sigma_0} - 1$ and figure 15 shows the graphs of the evolution of the vorticity $\zeta = \nabla \times \mathbf{v}$ with the Keplerian profile subtracted. The 2D plots show the progression of the formation of planetary gap in figure 14(d). The addition of the planet at r_0 created a density bump and spiral waves were formed. A couple of vortices could be clearly seen in the 50th period, as observed in figure 14 and figure 15. The planetary gap became clearer and wider in the 250th period and the 500th period, while the vortices beyond the gap merged into one. As a result, angular momentum were transported and eventually leading to accretion.

Figure 16 shows the graphs of surface density pertur-

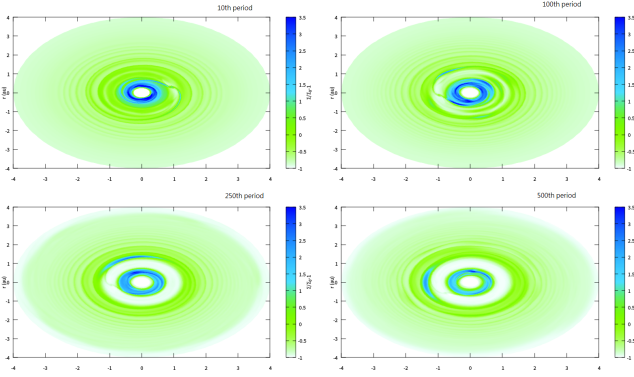


FIG. 14: The 2D plots of surface density perturbation $\frac{\Sigma}{\Sigma_0} - 1$ at different periods with $\tau = 0$.

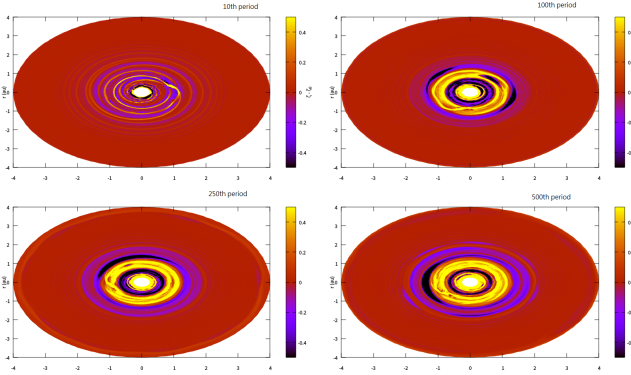


FIG. 15: The 2D plots of vorticity deviated from the initial profile $\zeta - \zeta_0$ at different periods where $\zeta = \nabla \times \mathbf{v}$.

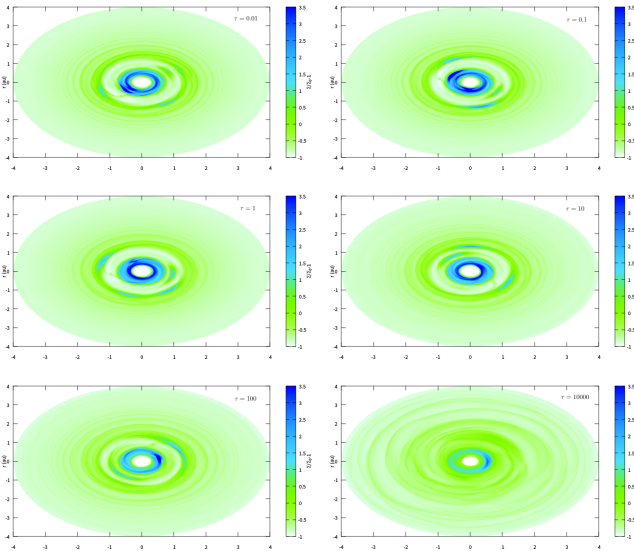


FIG. 16: The 2D plots of surface density perturbation $\frac{\Sigma}{\Sigma_0} - 1$ at the 100th orbital period with different thermal relaxation timescales τ .

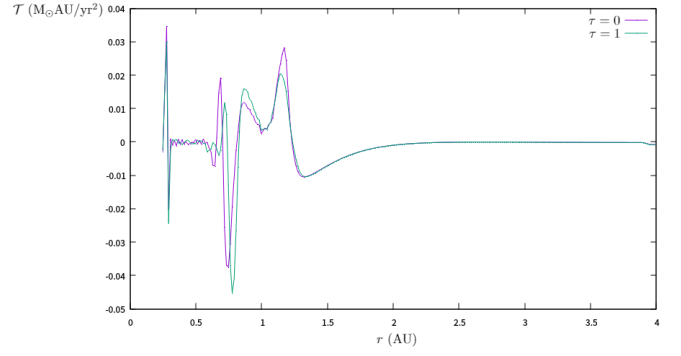


FIG. 17: The plots of the radial profile of \mathcal{T} at the first period with $\tau = 0$ and $\tau = 1$.

bation at the 100th orbital period using different thermal relaxation timescale τ . For lower τ , the cooling rate is faster and the heat is transferred more efficiently, approaching the isothermal case where $\tau = 0$. On the other hand, heat is retained when vortices is induced by the planet addition. Figure 16 confirms this phenomenon as the case with $\tau = 10000$ shows the slowest vortices amplification and gap formation. The simulation with $\tau = 100$ and $\tau = 10$ showing the early stage of planetary gap formation, while the simulation for $\tau \leq 1$ show the vortices formed already after the same number of period.

By using eq (11) and eq (12), the following relation considering the angular momentum $\langle \Sigma v_\phi r \rangle$ could be obtained:

$$\frac{\partial \langle \Sigma v_\phi r \rangle}{\partial t} + \frac{1}{r} \frac{\partial \langle \Sigma v_\phi v_r r \rangle}{\partial r} = 0, \quad (23)$$

where $\langle \cdot \rangle$ is the azimuthally integrated value. Integrating eq (23),

$$\frac{\partial}{\partial t} \int_{disk} \langle \Sigma v_\phi r \rangle = - \langle \Sigma v_\phi v_r r \rangle, \quad (24)$$

which refers to the conservation of angular momentum. For outward angular momentum transport, the condition:

$$\mathcal{T} \equiv \langle \Sigma v_\phi v_r r \rangle > 0 \quad (25)$$

could be obtained, angular momentum is gained and the mass moves inward. In contrast, for $\mathcal{T} < 0$, the angular momentum is lost and the mass moves away from the center.

Figure 17 shows \mathcal{T} against r with $\tau = 0$ and $\tau = 1$ at the first period. The figure shows the transport rate of angular momentum was faster in the isothermal case in general. Figure 18 and figure 19 show the curves of \mathcal{T} against r with $\tau = 0$ at the 5th and the 50th period respectively. The planet was not added into the system to investigate if there was any momentum transport in the Keplerian disk with a central star. Angular momentum transport only occurred near the boundaries since the outflow boundary conditions allow matter to move

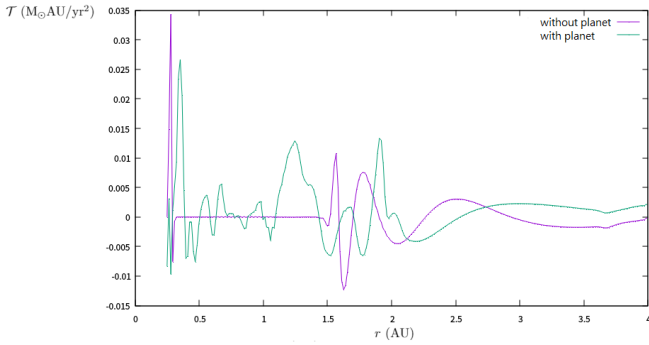


FIG. 18: The plots of the radial profile of \mathcal{T} at the 5th period with $\tau = 0$, comparing the effect of whether a planet was added to the system.

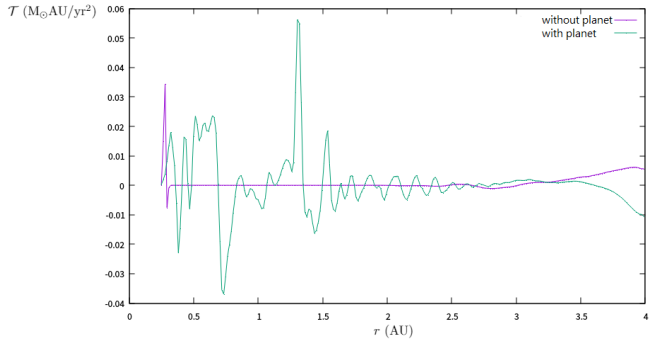


FIG. 19: The plots of the radial profile of \mathcal{T} at the 50th period with $\tau = 0$. The sub-figures (a) and (b) show the case of without or with the planet added to the disk respectively.

into the ghost zone of the disks. At the 50th period, figure 19 confirms there was no accretion and the disk was in equilibrium.

In order to investigate if the boundary conditions affect the transport of momentum inside the disk, simulations were made using reflective boundaries in the radial direction.

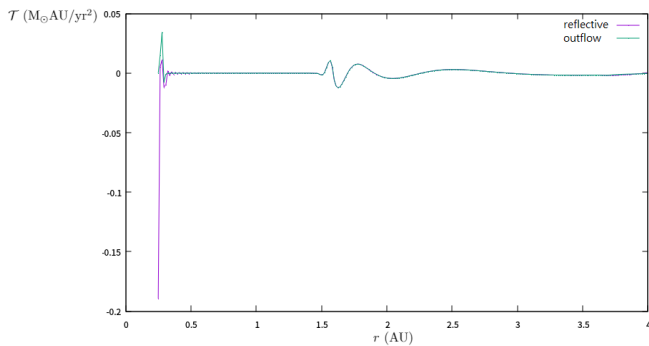


FIG. 20: The plots of the radial profile of \mathcal{T} at the 5th period with $\tau = 0$ without the planet added using different boundary conditions.

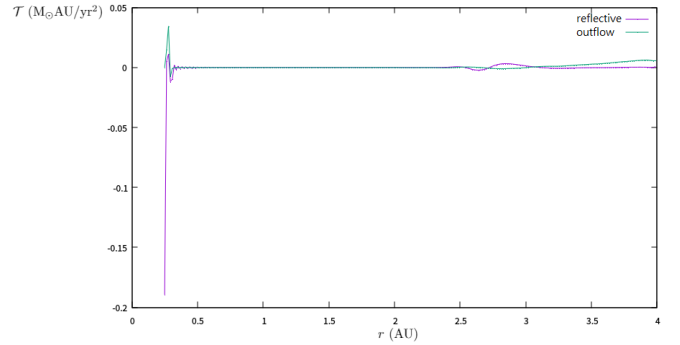


FIG. 21: The plots of the radial profile of \mathcal{T} at the 50th period with $\tau = 0$ without the planet added using different boundary conditions.

Figure 20 and figure 21 compare the results of using the reflective boundary conditions and outflow boundary conditions in radial direction at 5th and 50th orbital period respectively. The directions of the angular momentum transported of the cases in the boundaries were in opposite. Moreover, negligible transport of angular momentum were found inside the disk for the simulation without adding a planet.

A. Assumption validity

1. Viscosity

Neglecting viscosity may influence the mass transport, thus reducing the lifetime of the vortices. For the inviscid approximation, the viscosity is turbulent-triggered by the RWI. However, the approximation avoid the undesirable effect of viscous heating.

2. Self Gravity

Self Gravity is neglected since the tidal gravity of the disc was not strong enough (Bambi, 2016). The argument is related to the Toomre parameter $Q \equiv \frac{c_s v_K}{\pi G \Sigma r}$. With the initialization values considered in the previous sections, the self gravity could be neglected since $Q \gg 1$. However, if the mass of the disc changes or the disc is very close to the central star, self-gravitational force should be considered since the tidal effect is significant. This is also the reason of the domain of (0.25, 4.0) considered.

3. Thin disk and 2D approximation

In reality, the disk is 3D and there is thickness of the disk. Some vertical effects such as the vertical convection may not be accounted. In general, the thickness of the accretion is not constant and the vertical structure will affect the vortex pattern (Meheut et al., 2010).

B. Possible simulation exploration

Another method to trigger RWI is to add perturbation to the initial surface density profile. The advantage of the method is to control the unstable mode, which in fact is the wavenumber in eq (6), such that the growth rate could be calculated for each mode to investigate in the linear growth of the system.

Mehuet et al. (2012) performed the accretion disk simulation using such method to investigate the linear phase of RWI and the nonlinear evolution.

VI. CONCLUSION AND OUTLOOK

The Rossby Wave Instability was theoretically and numerically studied to investigate the mechanism of angular momentum transport which leads to accretion. RWI was triggered by a local density bump in a geometrically thin, inviscid, non self-gravitating disk with a planet added initially to the disk. The system evolved using the basic fluid dynamics equations and the planet position was updated using leapfrog integrator, while a thermal relaxation algorithm was implemented in order to study the efficiency of the cooling effect. The processes of accretion were investigated for different values of thermal relaxation timescale τ and a simple argument for the angular momentum transport was made and verified.

The accretion disk in this simulation is idealized and assumptions are made. There are 3D effects and different perturbations which may affect the system. While it is computationally expensive, the simulation could be conducted in higher resolution and larger number of orbits in order to investigate in the later times, such as the nonlinear phase of the instability. In addition, the RWI could be compared to the other models considering angular momentum transport, where the flow is assumed to be viscous and the transport in angular momentum is at smaller scales.

VII. ACKNOWLEDGEMENT

The author wishes to thank Dr. P. K. Leung from Department of Physics, The Chinese University of Hong Kong to give advice for the project.

VIII. REFERENCES

- Bambi C. (2016). *Astrophysics of Black Holes: From Fundamental Aspects to Latest Developments* (Springer).
- Johnathan W. (2014). "Planet formation captured in photo". *BBC News*.
- Les R. & Lin M. K. (2015). Gap formation and stability in non-isothermal protoplanetary discs, 1503-1513.
- Koller J., Li H. & Lin D. N. C. (2003). Vortices in the co-orbital region of an embedded protoplanet. *The Astrophysical Journal Letters*, 596, L91
- Li H., Finn J. M., Lovelace R. V. E. & Colgate S. A. (2000). Rossby Wave Instability of Thin Accretion Disks. II. Detailed Linear Theory. *The Astrophysical Journal*. 533(2), 1023-1034.
- Lin H., Barranco J.A., & Marcus P. S. (2002). Vortex dynamics and angular momentum transport in accretion disks. *Center for Turbulence Research Annual Research Briefs*, 289-299.
- Lobo Gomes A., Klahr H., Lucia Uribe A., Pinlla P. & Surville C. (2015). Vortex Formation and Evolution in Planet Harboring Disks under Thermal Relaxation. *The Astrophysical Journal*. 810(2).
- Lovelace R. V. E., Li H. , Colgate S. A. & Nelson A. F. (1999). Rossby Wave Instability of Keplerian Accretion Disks. *The Astrophysical Journal*. 513(2).
- Lovelace R. V. E. & Romanova M. M. (2013). Rossby Wave Instability in Astrophysical Discs. *Fluid Dynamics Research*. 46(4).
- Meheut H., Lovelace R.V.E. & Lai D.(2012). How strong are the Rossby vortices?. *Monthly Notices of the Royal Astronomical Society*. 430(3), 1988-1993.
- Meheut H., Casse F., Varnière P. & Tagger M. (2010). Rossby wave instability and three-dimensional vortices in accretion disks. *Astronomy and Astrophysics*. 516(4).
- Mignone A., Bodo G., Massaglia S., Matsakos T., Tesileanu O., Zanni C. & Ferrari, A. (2007). PLUTO: A Numerical Code for Computational Astrophysics. *The Astrophysical Journal Supplement Series*. 170(1), 228-242.
- Müller T. W. A., Kley W. & Meru F. (2012). Treating gravity in thin-disk simulations. *Astronomy Astrophysics*. 541, A123.
- Tagger M. & Varnière P. (2006). Reviving Dead Zones in accretion disks by Rossby vortices at their boundaries. *Astronomy Astrophysics*. 446(2).
- Thompson, M. J. (2006). *An Introduction to Astrophysical Fluid Dynamics* (Imperial College Press:London).